Volume 12
Number 35
21 September 2024
Pages 8479–8802

Journal of Materials Chemistry B

Materials for biology and medicine

rsc.li/materials-b

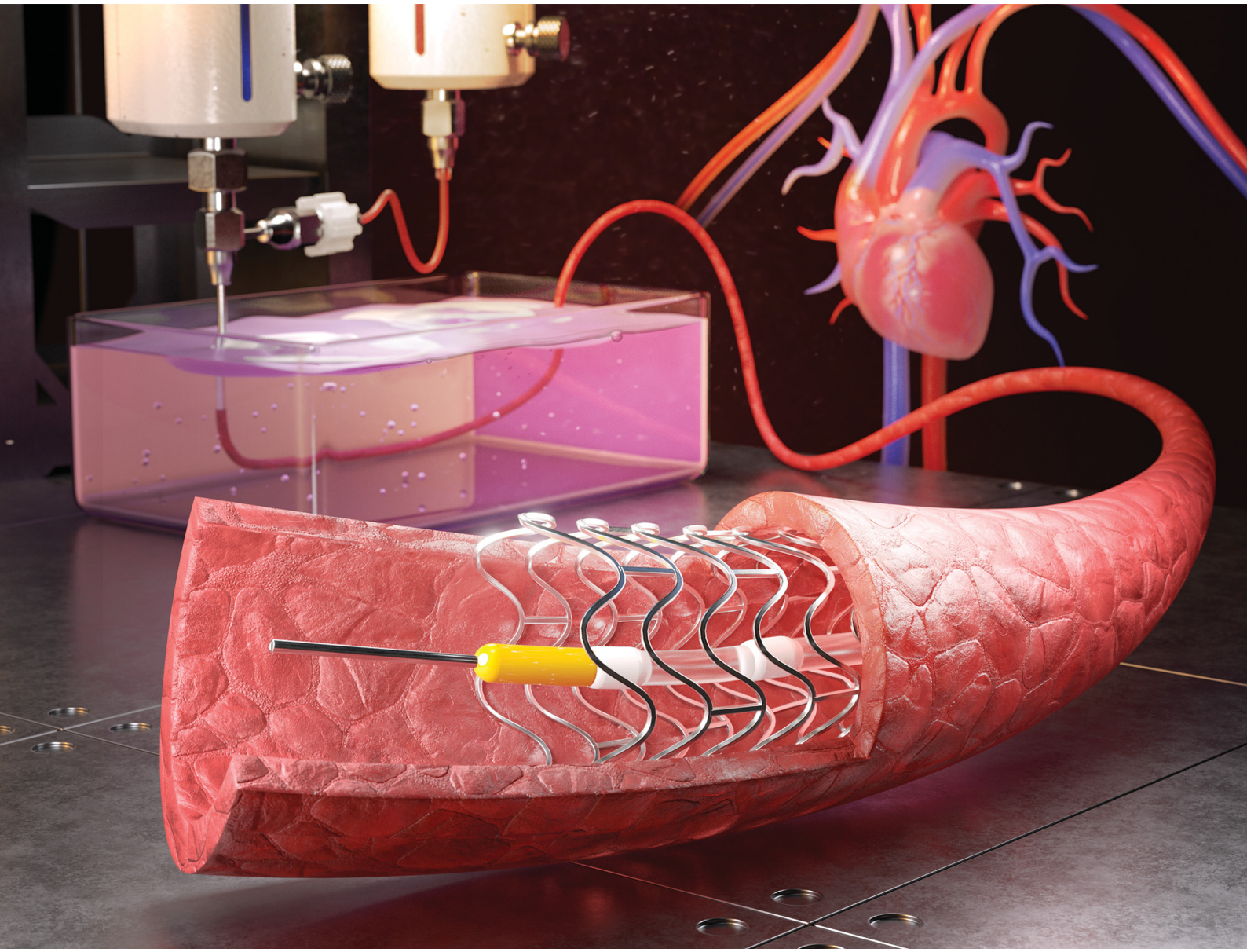

ISSN 2050-750X

ROYAL SOCIETY OF CHEMISTRY

PAPER

Yeong-Jin Choi, Hee-Gyeong Yi *et al.*
Coaxial bioprinting of a stentable and endothelialized human coronary artery-sized *in vitro* model

Journal of Materials Chemistry B

ROYAL SOCIETY OF CHEMISTRY

PAPER

View Article Online
View Journal | View Issue

Cite this: J. Mater. Chem. B, 2024, 12, 8633

Coaxial bioprinting of a stentable and endothelialized human coronary artery-sized *in vitro* model†

Ashfaq Ahmad,[ab] Seon-Jin Kim,[c] Yun-Jin Jeong,[d] Muhammad Soban Khan,[e] Jinsoo Park,[e] Dong-Weon Lee,[e] Changho Lee,[fg] Yeong-Jin Choi*[hi] and Hee-Gyeong Yi*[ab]

Atherosclerosis accounts for two-thirds of deaths attributed to cardiovascular diseases, which continue to be the leading cause of mortality. Current clinical management strategies for atherosclerosis, such as angioplasty with stenting, face numerous challenges, including restenosis and late thrombosis. Smart stents, integrated with sensors that can monitor cardiovascular health in real-time, are being developed to overcome these limitations. This development necessitates rigorous preclinical trials on either animal models or *in vitro* models. Despite efforts being made, a suitable human-scale *in vitro* model compatible with a cardiovascular stent has remained elusive. To address this need, this study utilizes an in-bath bioprinting method to create a human-scale, freestanding *in vitro* model compatible with cardiovascular stents. Using a coaxial nozzle, a tubular structure of human coronary artery (HCA) size is bioprinted with a collagen-based bioink, ensuring good biocompatibility and suitable rheological properties for printing. We precisely replicated the dimensions of the HCA, including its internal diameter and wall thickness, and simulated the vascular barrier functionality. To simplify post-processing, a pumpless perfusion bioreactor is fabricated to culture a HCA-sized model, eliminating the need for a peristaltic pump and enabling scalability for high-throughput production. This model is expected to accelerate stent development in the future.

Received 22nd March 2024,
Accepted 5th July 2024

DOI: 10.1039/d4tb00601a

rsc.li/materials-b

1. Introduction

Cardiovascular diseases (CVDs) constitute the leading global cause of mortalities. In 2010, they were responsible for approximately 16.7 million fatalities worldwide, and projections indicate a staggering estimate of 23.3 million deaths by 2030.[1] According to the World Health Organization, in 2019, an estimated 17.9 million individuals succumbed to CVDs, constituting 32% of all global mortalities.[2] Among these CVD-related deaths in 2019, approximately 7.4 million (approximately 42%) were attributed to coronary heart disease, while 6.7 million (approximately 38%) were associated with stroke. These conditions arise as a consequence of complications from atherosclerosis[3] and are characterized by the accumulation of plaques within the arteries.[4] The gradual narrowing and rigidity of blood vessels caused by the presence of atherosclerotic plaques restricts the efficient circulation of blood and the supply of oxygen to tissues. If not addressed, this can potentially result in critical medical emergencies.[5] In the early stages, atherosclerosis can be controlled through lifestyle modifications and medication.[6] The current clinical approach used to treat advanced atherosclerotic plaques involves minimally invasive techniques, such as angioplasty with stenting to reopen narrowed arteries, and atherectomy to enhance stent placement success.[7] Additionally, more invasive procedures like coronary bypass surgery are typically reserved for very

[a] Department of Convergence Biosystems Engineering, Chonnam National University, Gwangju, 61186, Republic of Korea. E-mail: hgyi@jnu.ac.kr
[b] Interdisciplinary Program in IT-Bio Convergence System, Chonnam National University, Republic of Korea
[c] School of Interdisciplinary Bioscience and Bioengineering, Pohang University of Science and Technology (POSTECH), Pohang, 37666, Republic of Korea
[d] Department of Automatic System, Chosun College of Science & Technology, Gwangju, 61453, Republic of Korea
[e] Department of Mechanical Engineering, Chonnam National University, Gwangju, 61186, Republic of Korea
[f] Department of Artificial Intelligence Convergence, Chonnam National University, Gwangju, 61186, Republic of Korea
[g] Department of Nuclear Medicine, Chonnam National University Medical School and Hwasun Hospital, 58128, Republic of Korea
[h] Bio and Healthcare Materials Research Division, Korea Institute of Materials Science (KIMS), Changwon, 51508, Republic of Korea. E-mail: jinchoi@kims.re.kr
[i] Advanced Materials Engineering, Korea National University of Science and Technology (UST), Republic of Korea

† Electronic supplementary information (ESI) available. See DOI: https://doi.org/10.1039/d4tb00601a

advanced-stage emergencies.[8] However, current strategies for managing atherosclerosis, such as angioplasty and percutaneous bypass surgery, pose invasiveness-related risks and do not fully address the underlying inflammatory pathology.[9,10] Despite the advancement of these treatments, patients remain susceptible to restenosis and ongoing plaque development.[11,12] Moreover, a one-size-fits-all approach to therapy disregards the unique variations in the disease's root causes.[13] The use of patient-specific blood flow simulations in arteries is under consideration as a promising method for improving diagnostics and treating heart-related diseases.[14] Smart stents with an integrated sensor for detecting in-stent restenosis and heart dynamics are being developed, demonstrating high-structural integrity, durability, and real-time monitoring capabilities in phantom models.[15,16] Furthermore, stents with integrated passive pressure sensors are being developed for real-time cardiovascular pressure monitoring.[17] Validating these new technologies requires rigorous preclinical testing using either *in vitro* or animal models to ensure safety and efficacy before human applications. Typical, two-dimensional, *in vitro* models often lack the three-dimensional complexity, blood flow simulations, cell-to-cell interactions, or an extracellular matrix environment found in living tissues.[18] Although animal studies offer a physiological context they face limitations in isolating specific elements of tissue environments[19] relevant to vascular diseases. Additionally, notable anatomical differences between human and animal models can result in species-specific variations. A clear example is observed during pregnancy, where the processes regulating the transformation of spiral arteries to deliver nutrients to the placenta and fetus differ significantly between humans and mice.[20] Moreover, substantial differences in arterial blood pressure, threefold greater elasticity, and differences in vessel sizes relative to the size of the heart were observed in larger animal models (such as swine) compared to humans; these could lead to underestimations of wall stress and other physiological factors.[21–23] Therefore, there is a pressing need for an advanced, human-scale model to recapitulate accurately the dimensions and physiology of coronary arteries.

Following the recent advancements in tissue engineering and the evolution of new technologies, notable initiatives have been documented that aim to create highly accurate *in vitro* vascular platforms for various applications.[24] Some key methods used to create a blood vessel *in vitro* platform include scaffold-based fabrication.[25] This method involves seeding vascular cells onto natural or synthetic scaffolds to produce tubular tissue-engineered blood vessels, with materials like collagen, fibrin, and decellularized vessel matrices. The self-assembly method[26] induces endothelial and smooth muscle cells to form concentric tubular structures spontaneously under appropriate culture conditions. Microfluidic systems[27] create endothelialized vascular channels within microfluidic devices, subjecting them to controlled hemodynamic stresses. Decellularization/recellularization[28] involves the removal of cells from donor blood vessels and repopulating them with autologous cells to create personalized grafts. However, none of these methods have successfully replicated the dimensions of HCA, particularly the variation in their sizes. In terms of vessel diameter, the right coronary artery sizes typically range from 1.8 to 6.2 mm,[29] while the diameter of the left coronary artery ranges from 2 mm to 7.3 mm,[30] depending on its location. The inner diameter of commonly used coronary artery stents typically falls within the range of 2.5–4 mm.[31,32] Additionally, the wall thickness of the native coronary artery ranges from 300 μm to 1000 μm.[33]

The advancements in three-dimensional (3D) bioprinting technologies, specifically those related to coaxial nozzle technologies, enable the precise deposition of cells and biomaterials in a concentric fashion, mimicking the structural and functional characteristics of vascular tissues. For instance, Gao *et al.*[34] used a coaxial nozzle to construct an *in vitro* vascular model with an internal diameter of around 1 mm. This accurately reproduced the pathophysiological characteristics of the vascular endothelium, as the endothelium plays a pivotal role in the majority of vessel-related pathologies.[35] However, relying on peristaltic pumps for perfusion complicates the scalability of these *in vitro* platforms to high-throughput systems.

The primary aim of this study was to develop an HCA-sized *in vitro* model that mimics its dimensions, specifically targeting an internal diameter of approximately 3 mm and wall thickness ranging from 300 μm to 1000 μm where it can hold a cardiovascular stent. We formulated and optimized a bioink suitable for coaxial printing, resulting in the creation of a well-defined tubular structure while maintaining its compatibility to facilitate endothelialization. Using a coaxial nozzle, we varied the wall thickness of the endothelialized model across a desired range by manipulating printing parameters. Additionally, we fabricated a pumpless perfusion chamber designed for culturing the bioprinted tube without the necessity for extra pump equipment. This approach not only enhances scalability but also suggests its potential for adaptation to high-throughput platforms.

2. Methods

2.1. Cell culture

Human umbilical vein endothelial cells (HUVECs, Promocell) and green fluorescent protein (GFP)-expressing human umbilical vein endothelial cells (GFP-HUVECs) were used for endothelialization. The cells were cultured in ready-to-use endothelial cell growth medium 2, which includes basal medium and supplement mix (Promocell), along with 1% penicillin–streptomycin (Hyclone). The cell cultures were maintained at 37 °C in a 5% CO_2 environment. To eliminate dead cells, the cultures were washed with Dulbecco's phosphate-buffered saline (DPBS) and the culture medium was refreshed every other day. Extended cultures were conducted until the cells reached 90% confluency. Cells were washed with DPBS twice, and then they were detached by incubating with 0.25% trypsin-EDTA (Promocell) for 180 seconds at 37 °C in a 5% CO_2 environment. The cells were then pelleted by centrifugation at 200 × *g* for 3 minutes at 25 °C. After discarding the supernatant of the cell suspension, the cells were either sub-cultured or used for

endothelialization experiments. For this study, cells between passages 3 and 5 were used.

2.2. Bioink preparation

To formulate a hybrid bioink, collagen type-1 (Atellocollagen, Dalim Tissen) was combined with sodium alginate (Sigma-Aldrich) in acetic acid (0.5 M, Biosesang) and stirred together using a magnetic stirrer for at least 72 hours at 4 °C until the collagen fibers were completely dissolved, thus resulting in a homogeneous pre-gel solution. This pre-gel solution was filtered with a 40 μm cell strainer to remove undissolved collagen and was then neutralized using an NaOH solution (10 N, Biosesang) and supplemented with 10× PBS (Biosesang) to maintain osmotic balance. The final volume was adjusted using distilled water. The neutralized pre-gel solution was stored at 4 °C until use. To optimize the bioink formulation, different proportions of collagen and alginate were mixed to achieve the final concentrations of 1%, 2%, and 3% collagen combined with 2% alginate in the hybrid bioink. These formulations were labeled as 1C2A, 2C2A and 3C2A, respectively. Additionally, 2% alginate served as the negative control. PF-127 (Sigma-Aldrich) was dissolved in a 100 mM calcium chloride ($CaCl_2$) solution (Biosesang) to create fugitive ink at concentrations of 30% and 40%, labeled as CPF30 and CPF40, respectively.

2.3. Rheological characterization of bioink

The rheological properties of the hybrid bioink were analyzed using the Advanced Rheometric Expansion System (TA Instruments) using a plate geometry with a diameter of 22 mm. We measured the change in viscosity of the bioink at increasing shear rates at 5 °C. To evaluate complete gelation, the bioink was incubated at 37 °C for 30 min after it underwent ionic crosslinking. During this period, we observed changes in the gel's modulus. Additionally, a dynamic frequency sweep test was performed on the ionically crosslinked hydrogel, wherein both storage and loss moduli were assessed across a range of increasing angular frequencies.

2.4. Swelling behavior

The swelling behavior of the bioink was evaluated by casting hybrid bioink into wells of a 24-well plate (SPL Life Sciences) followed by dual crosslinking to form a gel disc. The gel disc was carefully transferred from the 24-well plate to a 6-well plate (SPL Life Sciences) and submerged in culture medium to allow swelling. Changes in the weight and diameter of the disc were monitored throughout the subsequent 72 h period.

2.5. Cell adhesion and proliferation test

To identify the optimal bioink formulation for endothelialization, we assessed cell adhesion and proliferation in the bioink groups described in Section 3.2. For cell adhesion, 0.1 million cells were seeded onto each bioink formulation group, and the adhesion area was quantified as the single cell spreading area after 6 h using the image analysis program Fiji/ImageJ (NIH). Cell proliferation was determined by counting the number of cells per unit area 72 h post-seeding. Additionally, cell proliferation was confirmed using the cell counting kit assay (CCK-8, GlpBio) at predetermined intervals according to the manufacturer's instructions.

2.6. Perfusion chamber fabrication and assembly

To establish a consistent media perfusion system for prolonged cell cultures, a pumpless perfusion chamber was designed using the computer-aided design software, Inventor (Autodesk, Inc.). This bottomless chamber comprised dual reservoirs, each with a 10 ml media holding capacity, a central chamber, and sealing zones designed for the immobilization of the tube. The chamber frame was 3D printed using polylactic acid (PLA) with a 3D printer (Sindoh). Following the printing process, the chamber frame was assembled with either a Petri dish or wide glass plate (76 × 52 mm, Matsunami) using silicon polymer, Sylgard 184 (Dow Corning) with a 10 : 1 ratio with its curing agent as a glue. To ensure the optimal fixation of the perfusion chamber, the fully assembled platform was carefully placed in a 60 °C oven overnight, allowing for the complete crosslinking of the glue.

2.7. 3D bioprinting using the coaxial nozzle technique

A customized coaxial nozzle (5G/9G, Ramé-Hart Instrument Co.) was connected to adjacent printheads of a multihead 3D bioprinter (T&R Biofab). Both the bioink (1C2A) and sacrificial ink (CPF40) were loaded into printheads connected with a pneumatic pressure system. Both were maintained at 5 °C and 37 °C for 15 min before printing to prevent the crosslinking of the hybrid bioink and to induce the solidification of the sacrificial ink, respectively. The CPF30 bath material was kept at 4 °C before printing. Immediately before printing, the material bath was briefly brought to room temperature, and the printing process was expedited to ensure that the gelation of the bath material embraced the structure inside it. During extrusion, the diffused Ca^{2+} ions from the core CPF40 rapidly crosslinked the alginate component of the hybrid bioink in the shell area, and as soon as the tube came in contact with the bath material, the diffusion of Ca^{2+} ions from the bath material (CPF30) swiftly triggered the complete crosslinking of the alginate on the outer surface of the tube (which remained uncrosslinked due to the limited diffusion of Ca^{2+} ions from the core CPF40) to form a robust tube. The printed structure was then incubated at 37 °C for 1 hour to allow complete collagen gelation within the hybrid biomaterial. After incubation, both ends of the structure were trimmed, and the tube was immersed in 1× PBS and was maintained at 4 °C for 1 hour to liquefy the water-soluble sacrificial material, resulting in the formation of a hollow, perfusable tube.

2.8. Endothelialization

Endothelialization of a hollow, acellular, perfusable tubular structure was achieved by mounting it on a perfusion chamber. The sealing zone of the chamber was cast with a mixture of SE1700 (Dow Corning) and polydimethylsiloxane (PDMS, Dow Corning) at 5 : 5 and 10 : 1 ratios with their respective curing agents, ensuring appropriate sealing and preventing

any leakage of the culture medium into the central chamber during the culture process. The tube was subsequently perfused with DMEM F12 (Gibco) containing 1% Matrigel (Corning) and maintained inside a humidified CO_2 incubator (37 °C) overnight. This step prepared the lumen of the tube for the attachment of cells by removing all remaining traces of CPF40. Furthermore, the silicon glue at the sealing zones also underwent appropriate curing during this time. On the subsequent day, HUVECs were trypsinized, counted, and resuspended at a density of 10 million cells per mL in a culture medium that contained 0.5% gelatin (Sigma-Aldrich) to enhance their settlement on the tube's lumen. After washing the tube with PBS, the outlet side of the chamber was sealed with noncytotoxic, pressure-sensitive, silicone adhesive polyethylene terephthalate PET tape (3 M). The cell suspension was introduced into the lumen through the inlet with the chamber tilted to prevent the cell suspension from leaking back. The inlet was immediately sealed with adhesive tape. Concurrently, a prewarmed solution of 10% GelMA (3D Materials) with 0.1% lithium phenyl-2,4,6-trimethylbenzoylphosphinate (LAP) was poured into the central chamber and readily subjected to photocrosslinking using ultraviolet light (UV) at a wavelength of 405 nm for a duration of 120 seconds to fully embed the tubular structure. The entire assembly was then placed in an incubator and the entire device was flipped at 180° after 2 hours for uniform cell adhesion on both sides of the lumen. After 3 hours, the tapes at the inlet and outlet were removed, and 1× PBS was perfused through the lumen to wash out nonadherent cells. Fresh culture medium was added to both reservoirs, and the chamber was placed on a two-dimensional rocker with an adjustable tilt angle, rocking at 5 rpm inside a 37 °C incubator with 5% CO_2. To sustain the endothelialization process, the culture medium was refreshed every other day.

2.9. Mechanical property assessment

To assess the ultimate tensile strength (UTS), after washing the core sacrificial CPF40, 20 mm long samples (n = 3) were securely immobilized between two clamps of a tensile testing machine (MCT-1150, A&D Company Ltd, Japan) at a crosshead speed of 2 mm min^{-1}, without any preconditioning or initial stretching. UTS was calculated as the maximum force sustained before tensile failure, divided by the cross-sectional area. Porcine left coronary artery (pLCA) and right coronary artery (pRCA) segments of similar length were harvested from a porcine heart obtained from a nearby slaughterhouse to use as controls. To evaluate the stentability, the samples were cultured for at least 3 weeks. A 3 mm diameter polycaprolactone (PCL) stent was then placed inside the lumen of each sample using a balloon inflator. After stent placement, Trypan blue was perfused through the samples to check for any leakage.

2.10. Computational fluid dynamics (CFD) simulation

A 3D tubular model was created using Fusion 360 (Autodesk) with an internal diameter (d) of 3 mm and a length of 50 mm. The numerical simulations for the fluid flow within the vascular tubular model were conducted using COMSOL Multiphysics (version 6.2, COMSOL Inc.). For the working fluid, Newtonian fluid was assumed with a density of 1000 kg m^{-3} and a dynamic viscosity (μ) of 0.00093 Pa s. The vascular walls were treated as rigid with a no-slip boundary condition. The effective height (h) of the media reservoir at each tilt angle, calculated using trigonometric relationships, was used to find the initial velocity (v) at the inlet using Torricelli's equation $\left(v = \sqrt{2gh}\right)$. The volumetric flow rate (Q) simulated through CFD was used to calculate wall shear stress (WSS) (τ_w) at each tilt angle using the Hagen–Poiseuille eqn (1).

$$\tau_w = 32\mu\frac{Q}{\pi d^3} \quad (1)$$

2.11. Permeability assay

To evaluate the endothelium's barrier function, fluorescein isothiocyanate (FITC)-conjugated dextran (70 kDa, Sigma-Aldrich) was perfused at a concentration of 0.1 mg mL^{-1} through the tube after 7 d of culture. We tracked the movement of these dextran molecules in the perivascular gel area around the tube using a fluorescent microscope (ZEISS). At regular intervals, images of a predefined region of interest (ROI) were captured. To calculate the diffusional permeability, we analyzed the variation in fluorescence intensity within this ROI over time, using the following eqn (2).

$$P_d = \frac{1}{I_{t_1} - I_b}\left(\frac{I_{t_2} - I_{t_1}}{t_2 - t_1}\right)\frac{d}{4} \quad (2)$$

where P_d represents the diffusional permeability coefficient, I_{t_1} denotes the average intensity measured at the initial time point t_1, I_{t_2} refers to the average intensity observed at a subsequent time t_2, I_b is the intensity due to background noise acquired before the introduction of FITC-Dextran, and d denotes the tube's diameter.

2.12. Immunofluorescence imaging

To confirm the endothelialization of the tube, after 7 days of culture, the tube was stained against CD31. Briefly, sections of the GelMA embedded tube were fixed in 4% paraformaldehyde (Biosesang) for 2 h and then permeabilized with 0.1% Triton X-100 (Biosesang) for 15 min at room temperature. To block any reactive epitopes, a solution of 10% fetal bovine serum (Gibco) in PBS was applied for 30 min. After washing with PBS, the samples were subsequently incubated with the primary antibody, anti-CD31 (Invitrogen), at 4 °C for 48 h. Following this, the samples were washed with PBS three times to remove any unbound primary antibodies. Subsequently, the samples were incubated with a secondary antibody conjugated with a fluorophore (Alexa flour 488 or Alexa flour 594) and counterstained with 4′,6-diamidino-2-phenylindole (DAPI) and phalloidin (Alexa flour 488 or Alexa flour 594), all at room temperature for 4 h. After labeling, the samples were imaged using a fluorescence microscope (ZEISS) and analyzed using ImageJ (NIH).

2.13. Statistical analysis

The experimental data were processed, the results were expressed as mean values ± standard deviations and were then plotted using Origin Lab and Microsoft Excel. For each condition, a minimum of three independent samples ($n \geq 3$) were analyzed to conduct statistical analyses. The Student's *t*-test was used to compare differences between the experimental groups.

3. Results and discussion

The study was designed to create an acellular tubular structure which can be populated with HUVECs for endothelialization. This was achieved through a microextrusion-based coaxial nozzle bioprinting system supported by a bath material to maintain the structural integrity of the tube and minimize the risk of collapsing (Fig. 1). The bioink was optimized in such a way that it maintained high printability, thus enabling the production of a target-sized tubular structure while retaining its endothelialization potential. This approach spares the cells from exposure to the high-pneumatic pressure typically required for extruding bioinks while maintaining good printability.[36] Furthermore, in this approach, postprocessing of the acellular tube immediately after printing is easier compared with a cell-laden tube, which carries a higher risk of contamination during postprocessing. Additionally, the acellular tube can be endothelialized more rapidly compared with direct printing approaches, wherein cells are encapsulated in bioinks and they must self-assemble in a two-dimensional cell monolayer for endothelium formation, which usually requires longer time.[34]

For the fabrication of a perfusable vascular model with precise dimensions *via* the coaxial bioprinting method, a bioink that crosslinks rapidly is essential. This requirement is key to achieving a well-defined tubular structure and reducing the risk of tube collapse during printing. Additionally, the bioink must possess appropriate mechanical and rheological properties to allow extrusion-based bioprinting. Considering these requirements, alginate-based hydrogels are deemed most suitable for this application due to their rapid ionic crosslinking mechanism and appropriate rheological properties governed by their widespread use in microextrusion-based bioprinting.[37–39] However, it is important to note that previous studies have identified native alginate as a bioinert material, characterized by a lack of mammalian cell-adhesive motifs and strong hydrophilicity, thus limiting its biological properties.[40–42] Although alginate lacks intrinsic domains for mammalian cell interaction, its composition and structure facilitate the creation of biomaterials well-suited for biomedical applications.[43] Rapid crosslinking of alginate-based hydrogels has been demonstrated to effectively produce hollow, perfusable tubes using coaxial nozzle systems without significantly affecting cellular functionality.[34,37,44] Endothelial cells proliferate well in alginate-blended bioinks, retaining their ability to self-assemble into functional endothelium. Herein, we formulated a hybrid bioink by blending alginate with collagen, a naturally abundant structural protein (Fig. 2a). Collagen provides essential cell binding motifs and a nanostructured framework, crucial for effective cell–matrix interactions. Additionally, collagen, being the

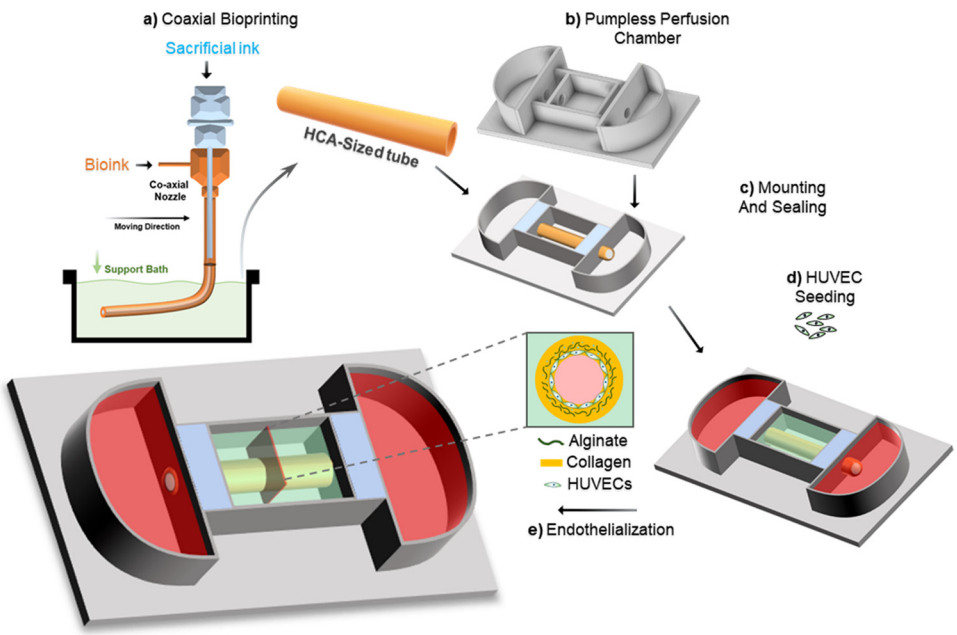

Fig. 1 Workflow schematic. (a) Bioprinting of an HCA-sized tube using a coaxial nozzle and a support bath. (b) Computer-aided design of a pumpless perfusion chamber. (c) Integration of a bioprinted HCA-sized tube with the pumpless perfusion chamber and complete sealing of the chamber. (d) GelMA embedding of the tube and seeding HUEVCs on its luminal surface for endothelialization. (e) Maturation and endothelialization on a pumpless perfusion platform.

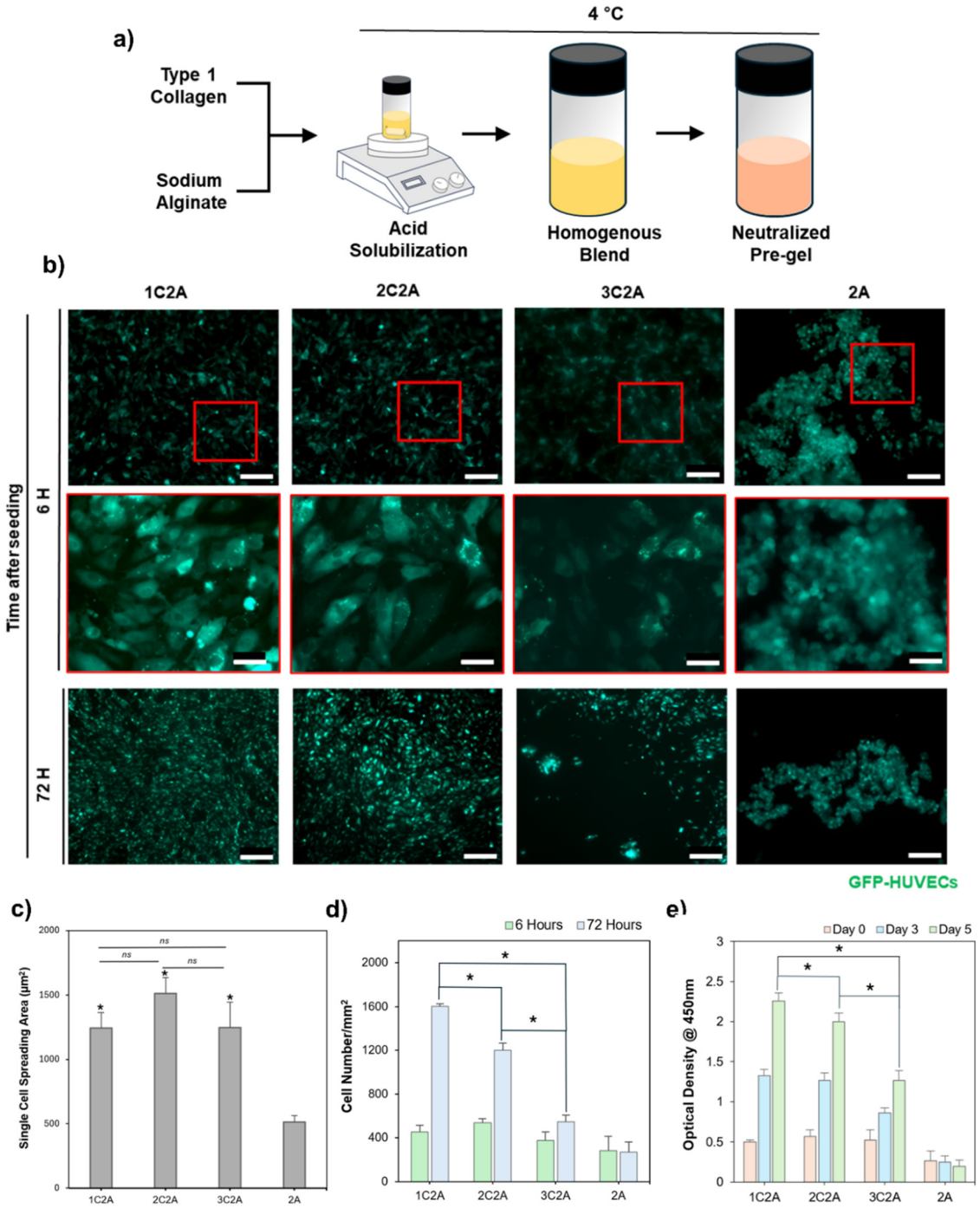

Fig. 2 Bioink preparation and evaluation of endothelialization potential. (a) Schematic illustration of the steps involved in composite bioink preparation. (b) Fluorescence microscopy images of green fluorescent protein-HUVECs seeded on the surface of different bioink compositions. Alginate (2%) served as a negative control. All bioink compositions supported HUVEC adhesion (scale bars: 200 μm, 50 μm for insets of the first row). (c) Quantification of the single-cell spreading area after 6 h of seeding. The symbol * indicates $p < 0.001$ *versus* 2A. (d) Significant differences were observed in cell proliferation, as quantified by counting the number of cells per unit area (*$p < 0.001$). (e) Cell proliferation was further confirmed by measuring optical density at days 0, 3, and 5 (*$p < 0.001$).

abundant protein in the extracellular matrix of native vascular tissues, offers an optimal environment for the growth and proliferation of vascular cells.[44] Collagen undergoes thermal crosslinking to form hydrogels at physiological temperatures.[45] Consequently, this hybrid bioink exhibits a dual crosslinking mechanism (Fig. 3a), making it highly compatible with the coaxial printing setup to yield a perfusable and robust tubular structure.

To identify the optimal bioink concentration for endothelial cell attachment and proliferation, we evaluated various hybrid bioink formulations. These formulations incrementally

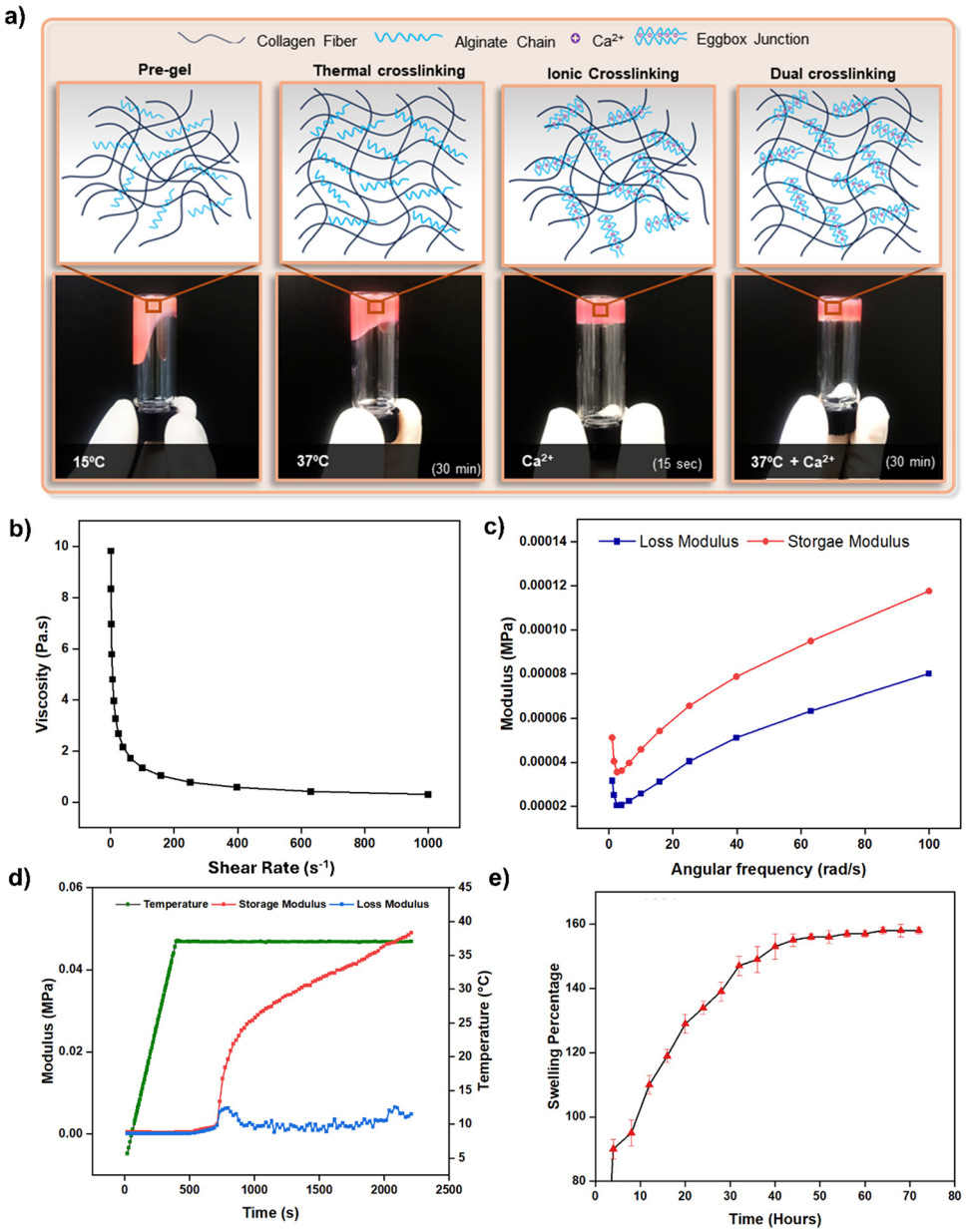

Fig. 3 Dual crosslinking mechanism, rheological properties, and swelling behavior of bioink. (a) Schematic illustration and gross images demonstrating the dual crosslinking mechanism of the bioink *via* the vial tilt method. (b) Viscosity measurements of the bioink at varying shear rates demonstrating the shear thinning behavior of bioink composition. (c) Dynamic frequency sweep analysis shows a higher storage modulus than the loss modulus of ionically crosslinked bioink across a range of angular frequencies. (d). Alteration in modulus upon subjecting the bioink to secondary thermal gelation at a physiological temperature. (e) Quantification of the swelling percentage of the 1C2A gel disc due to water uptake over a 72 h period.

increased the final collagen concentration from 1% to 3%, while the alginate concentration was maintained constant at 2%. This alginate concentration was chosen based on previous studies demonstrating its efficacy for fabricating freestanding vessels *via* a coaxial nozzle in a microextrusion-based bioprinter.[34] The formulations were labeled 1C2A, 2C2A, and 3C2A. Following crosslinking with calcium chloride (100 mM) and incubation at a physiological temperature (37 °C), endothelial cells were seeded on each formulation. We assessed the attachment area of individual cells after 6 hours, a period that is typically sufficient for endothelial cells to settle and adhere to substrates.[46] The results showed that all formulations facilitated endothelial cell adhesion with no significant differences observed among them (Fig. 2b and c). A 2% alginate solution was employed as a negative control. Interestingly, we observed that higher collagen concentrations in the hybrid bioink formulations led to decreased cell proliferation. This was quantified by measuring the number of cells per unit area 72 hours after seeding (Fig. 2d). The probable reason is that a denser network of collagen fibers combined with alginate led to reduced porosity, thereby hindering efficient cell proliferation. This observation is consistent with a previous report that indicated that dense

collagen networks can reduce cell proliferation.[47] This finding was confirmed based on the CCK8 assay outcomes at days 0, 3, and 5 after cell seeding (Fig. 2e). Considering its higher endothelialization potential, we decided to evaluate the rheological and swelling properties of 1C2A composition to check its suitability for use with a coaxial nozzle, aimed at fabricating hollow, tubular structures.

We investigated the bioink's rheological properties, such as viscosity and dynamic modulus, by subjecting it to ionic and thermal crosslinking, and by studying its swelling behavior. Due to the presence of thermally gelling collagen and ionically crosslinkable alginate, the hybrid composition (1C2A) underwent a dual crosslinking mechanism (Fig. 3a). To evaluate the gelation of this formulation, a vial tilting test was conducted following thermal, ionic, and combined (dual) crosslinking. Furthermore, we assessed how the viscosity of the 1C2A formulation changed under increasing shear rate conditions implemented at a controlled temperature of 5 °C. This specific temperature was chosen for the printing process to avoid any unwanted thermal crosslinking of the collagen within the bioink. The result demonstrates the shear-thinning characteristic of the 1C2A formulation (Fig. 3b). This shear-thinning property is essential in bioink formulation, particularly for use in microextrusion-based bioprinting systems. It imparts the bioinks with a suitable viscosity that facilitates a smooth flow through the printing nozzle and helps maintain the shape of the material after it has been deposited. Moreover, shear-thinning plays a vital role in ensuring the structural integrity and fidelity of the printed constructs, thus preventing any physical obstruction of the bioinks during their extrusion from the nozzle and aiding the effective retention of their designated shapes. The bioink formulation quickly formed a stable gel when subjected to ionic crosslinking, achieved by treating it with calcium chloride for a brief duration of 15 s (Fig. 3a). To evaluate the mechanical properties of the bioink after a brief (15 s) calcium chloride treatment, a dynamic frequency sweep analysis was conducted by measuring both the storage and loss moduli. The results showed that the ionically crosslinked bioink possessed gel-like mechanical properties instead of liquid-like properties. It further confirmed that the bioink was capable of maintaining its shape during the printing process, indicated by a higher storage modulus compared with the loss modulus (Fig. 3c). Furthermore, when the gel was exposed to a temperature of 37 °C, the storage modulus exhibited an additional increase, which can be attributed to the thermal crosslinking of collagen, thus suggesting that following dual crosslinking, the formation of a stable tubular structure was likely (Fig. 3d). Given that the swelling behavior of hydrogels due to water absorption in the culture medium can substantially modify the dimensions of the printed structure,[48] it is crucial to evaluate the swelling characteristics of the ink compositions. The swelling properties of the 1C2A composition were evaluated by first forming a gel disc in a 24-well plate, achieved through dual crosslinking. Subsequently, the disc was transferred to a 6-well plate and immersed in a medium to facilitate swelling. We monitored the disc's weight gain due to water absorption, and its diameter over the subsequent 72 h period. The gel disc exhibited rapid swelling for the first 40 h, increasing in size by up to 140% before it stabilized (Fig. 3d). During this phase, the disc's diameter expanded from 17 mm to 18.3 mm for 40 h of swelling and then remained stable during the subsequent hours (Fig. S1, ESI†). This observation suggests that minimal dimensional changes in the printed structure can be anticipated due to the swelling behavior of the bioink.

Before starting the coaxial bioprinting of tubular structures of a target size, we conducted a parametric study to understand the impact of variations in applied pressure to the shell and core nozzles, at a constant head speed, on the resulting luminal dimensions of the printed tube (Fig. 4a). These dimensions included the inner diameter and the wall thickness. The bioink composition exhibited shear-thinning properties that enabled us to effectively adjust the wall thickness of the printed tubular structure by altering the pneumatic pressure on the shell nozzle. We observed that increasing the shell pressure from 120 kPa to 160 kPa allowed the wall thickness to vary from 339 ± 41 μm to 976 ± 25 μm, consistent with the typical wall thicknesses of HCAs. As the pressure of the core nozzle remained constant, changes in the shell nozzle pressure not only altered the wall thickness but also the inner diameter of the tube. Consequently, the inner diameter of our printed structure decreased from 3121 ± 80 μm to 2948 ± 54 μm, which was within our targeted range (Fig. 4c). We opted to bioprint the tubular structure using a pressure of 140 kPa for the shell nozzle while we maintained a constant pressure of 65 kPa for the core nozzle. The printhead temperatures were critical in this process. Given the thermosensitivity of the collagen-containing shell bioink, its temperature was set to 5 °C. The core material (CPF40) is also thermosensitive and can liquefy at lower temperatures. Although it can retain its shape at room temperature, we maintained it at 37 °C to enhance its gel properties, aiming to achieve a more perfectly circular lumen after removal. Both temperatures were sustained for 10 min before loading the syringes into the printheads. Meanwhile, the CPF30 bath material was kept at 4 °C and was brought to room temperature immediately before printing. During printing, the alginate in the shell rapidly crosslinked upon contact with the calcium ions in the core CPF40 material (Fig. 4(b-i)). However, due to the limited diffusion of calcium ions, the outer layer of the alginate shell remained un-gelled, posing a risk of deforming the printed structure. This issue was resolved by adding calcium chloride to the bath material (Fig. 4(b-ii)). It ensured that the un-gelled alginate on the outer shell crosslinked through the diffusion of calcium ions from the bath, and thus resulted in a structurally sound, circular, freestanding tube (Fig. 4(b-iii)). The hollow tube was able to hold a 3 mm sized polycaprolactone (PCL) stent thus demonstrating the structure's compatibility with conventional cardiovascular stents after incubation at 37 °C (Fig. 4d). The mechanical properties of the printed tube were assessed through ultimate tensile strength (UTS) testing and compared with those of the porcine left coronary artery (pLCA) and right coronary artery (pRCA), which are common sites for stent

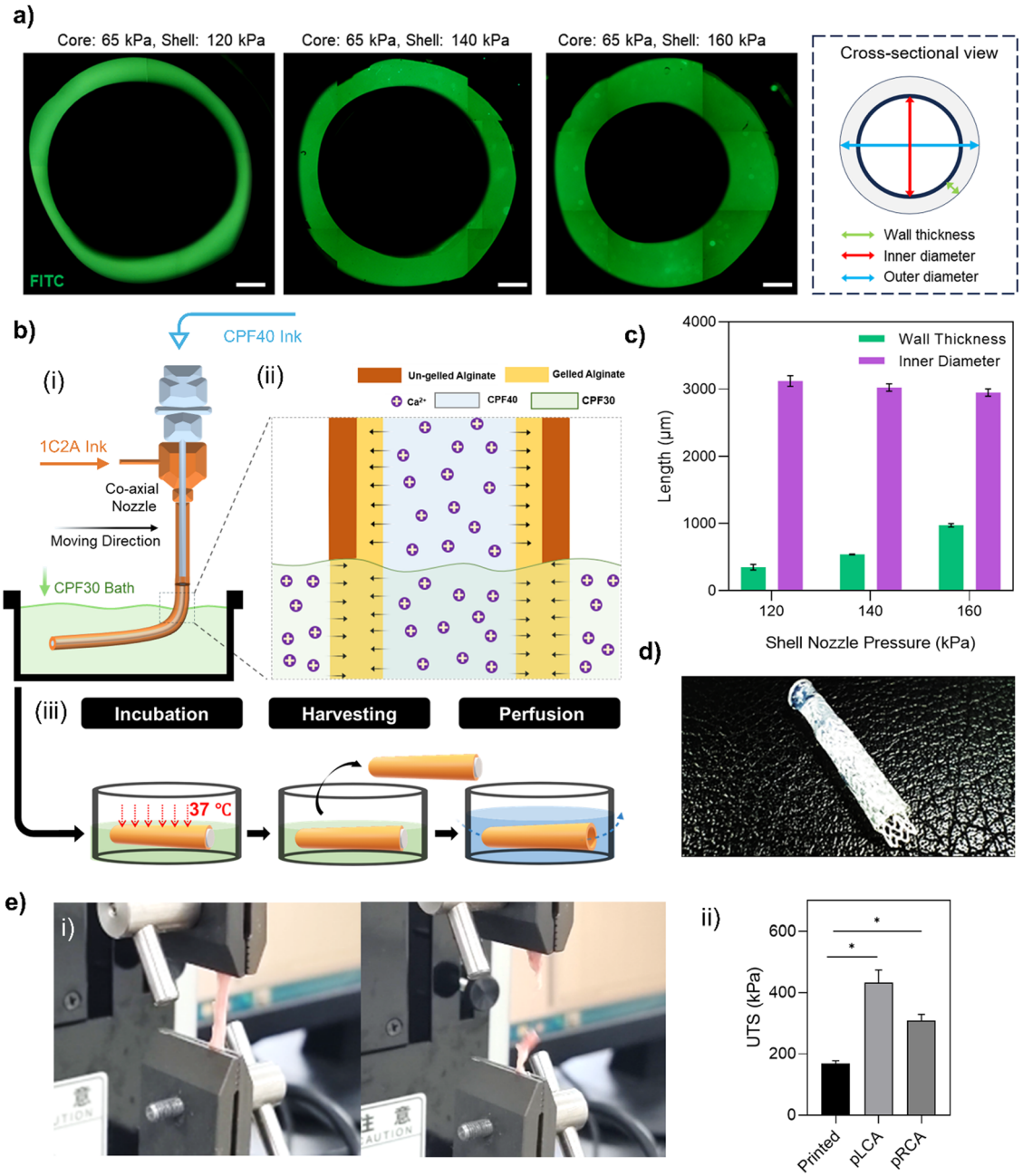

Fig. 4 Support bath-assisted coaxial bioprinting of the HCA-sized tube. (a) Cross-sectional view of printed tubular structures at varying shell-nozzle pressures. The wall thickness and inner diameter of the tube are controlled by the pressure in the shell nozzle, while the pressure in the core nozzle is kept constant (scale bars: 500 μm). (b) (i) Schematic illustration of microextrusion-based coaxial bioprinting, where 1C2A bioink is extruded through the shell part of the nozzle, CPF40 ink is extruded through the core part of the nozzle, and CPF30 is used as the bath material; (ii) rapid crosslinking mechanism through diffusion of Ca^{2+} ions from the core material and bath material to yield a robust tube; and (iii) post-printing steps until obtaining a hollow, perfusable tube. (c) Quantification of the changes in wall thickness and inner diameter of the printed tube by varying the pressure in the shell nozzle. (d) Gross image of the printed tube's ability to hold a PCL stent. (e) Ultimate tensile strength (UTS) test images showing the (i) tension and failure of samples. (ii) Compared to pLCA and pRCA, the printed tube had significantly less UTS (*$p < 0.05$).

placement in animal models[49] (Fig. 4(e-i)). The UTS of the printed tube (167 ± 10 kPa) was significantly lower than those of the pLCA (431 ± 42 kPa) and pRCA (308 ± 20 kPa) (Fig. 4(e-ii)). However, to determine if the printed tube could withstand the pressure exerted by a balloon inflator during the stent placement procedure, trypan blue was perfused through the tube after a stent was placed inside a 3-week cultured tube. Embedded within a supporting GelMA matrix, the tube was able to sustain the pressure applied by the balloon inflator without any leakage of trypan blue (Fig. 6 and Movie S1, ESI†).

Even though peristaltic pumps can effectively replicate hemodynamic flow within tubular structures,[50] their use limits

the scalability of *in vitro* models and constrains high-throughput testing. Consequently, we opted to endothelialize and culture the printed tubes using a pumpless perfusion chamber, which facilitates dynamic culture on a two-dimensional rocker. This chamber was specifically designed to house the tubular structure, with media chambers on each side for nutrient fluid. It also featured two sealing zones at both ends of the tube to secure them in place and prevent media leakage. We constructed a bottomless chamber framework using PCL, a material known to be biocompatible[51] and extensively used in 3D printing to

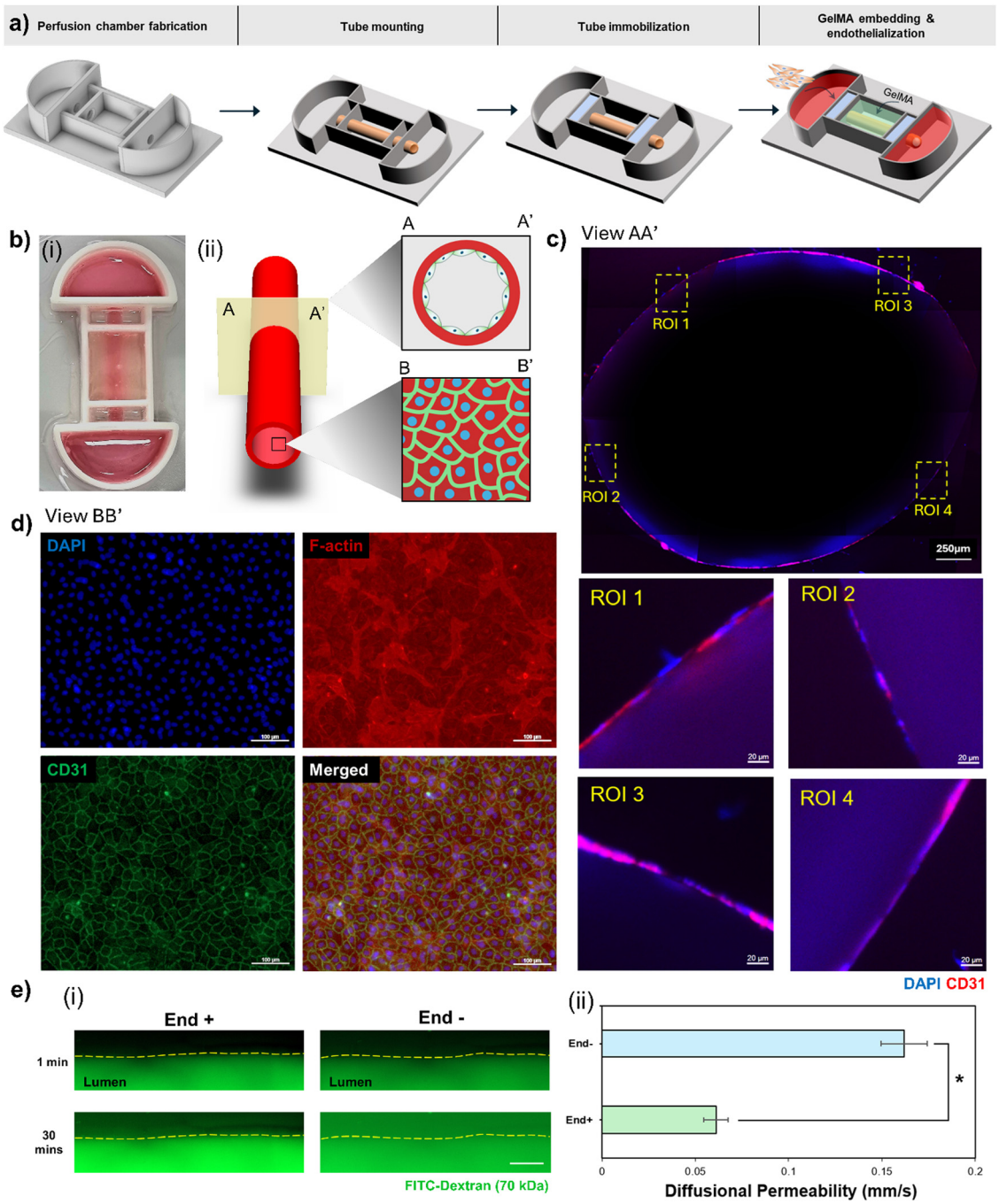

Fig. 5 Endothelialization of the tubular construct. (a) Schematic illustration of the steps involved in the endothelialization process, including perfusion chamber fabrication, tube mounting, immobilization, and seeding of HUVECs. (b) (i) Gross image of the immobilized tube and (ii) schematic of different views of the tubular structure observed after endothelialization. (c) Representative immunostained image along section AA′ and inset views at multiple ROI showing the uniform expression of CD31 on the luminal surface (scale bar: 250 μm; 20 μm for the insets). (d) View along section BB′ showing CD31 localization at cell junctions and the spread of actin filaments (scale bar: 100 μm). (e) (i) FITC-Dextran (70 kDa) perfusion through the tube: dashed lines distinguish the lumen from the perivascular gel region (scale bar: 200 μm); (ii) increased permeability of the tube without endothelium (End−), whereas the endothelialized tube (End+) maintains its barrier function, impeding the permeability of dextran molecules (*$p < 0.001$).

create complex three-dimensional structures with excellent shape fidelity.[52] We assembled the bottomless framework of the chamber using silicon glue to attach it to a transparent glass slide, as explained in Section 2.6. The tubular structure was then mounted and secured with silicon material. After silicon curing, the tubular structure was embedded in a 10% GelMA matrix (Fig. 5a). Although the tube can be securely fixed and immobilized within the chamber after printing, it is susceptible to deterioration over time due to the dissociation of alginate during the culturing process. The GelMA embedding matrix provides a supportive environment that prevents the collapse or damage of the tubular construct throughout the culture period (Fig. 5(b-i)). Additionally, the inherent transparency of GelMA is advantageous as it permits the observation and tracking of biomolecules. This attribute is particularly useful for terminal assays, such as permeability assays, where the movement of fluorescently labeled dextran can be monitored in the perivascular gel region. After seeding, HUVECs proliferate and mature into an endothelium on the luminal surface of the tube. This approach, unlike direct cell printing with cell-laden bioinks, protects the cells from the shear stress typically experienced during printing.[53] Given that the endothelium is present in the form of a two-dimensional endothelial monolayer rather than a three-dimensional network, encapsulation is not optimal.[54] This is because the cells need to remodel the extracellular matrix and migrate to the luminal surface to establish the endothelium. Consequently, in these cases, the stiffness of the matrix becomes a critical factor that requires careful optimization to support the self-assembly of HUVECs. While the cell seeding approach spares the cells from shear stress-induced damage compared to direct cell printing, it often raises concerns about achieving a uniform distribution of cells on the luminal surface. We examined cross-sectional and luminal surface views of the tube to assess cell distribution (Fig. 5(b-ii)). In the cross-sectional view of the endothelialized tube (Fig. 5c), we observed a uniform expression of CD31 along the entire luminal surface. This was confirmed by magnifying different ROIs on both the upper and lower luminal surfaces, indicating uniform cell distribution. After seven days of culture, we immunostained a section of the luminal surface of the tube. This staining revealed CD31 expression, localized primarily at the cell junction areas (Fig. 5d). This suggests that the HUVECs successfully formed a monolayer, thus establishing a selectively permeable barrier. This barrier is a critical function of the endothelium in arteries.

The barrier function of the endothelium within the tube was assessed by perfusing FITC-labeled dextran (70 kDa) as a permeability indicator. It was perfused through the tubular structure, and the resulting changes in fluorescence intensity in the surrounding perivascular gel were monitored over time (Fig. 5(e-i)). In tubes with endothelial cells (End+), a robust barrier function was observed, effectively limiting the permeability of dextran molecules into the perivascular gel area with a low-diffusional permeability of 0.061 ± 0.0065. In contrast, tubes lacking endothelial cells (End−) showed increased diffusional permeability (0.162 ± 0.0123) (Fig. 5(e-ii)). These outcomes suggest that the tube, with a size similar to those of HCAs, successfully replicates the native endothelium's barrier function.

Endothelial cells lining the lumen of arteries are highly mechanosensitive, possessing mechanoreceptors that enable them to detect mechanical forces, such as shear stress induced by blood flow. These forces are converted *via* mechanotransduction pathways into functional responses, such as adjusting vascular tone or activating an inflammatory response.[55] Although we simplified the induction of flow using a gravity-driven,

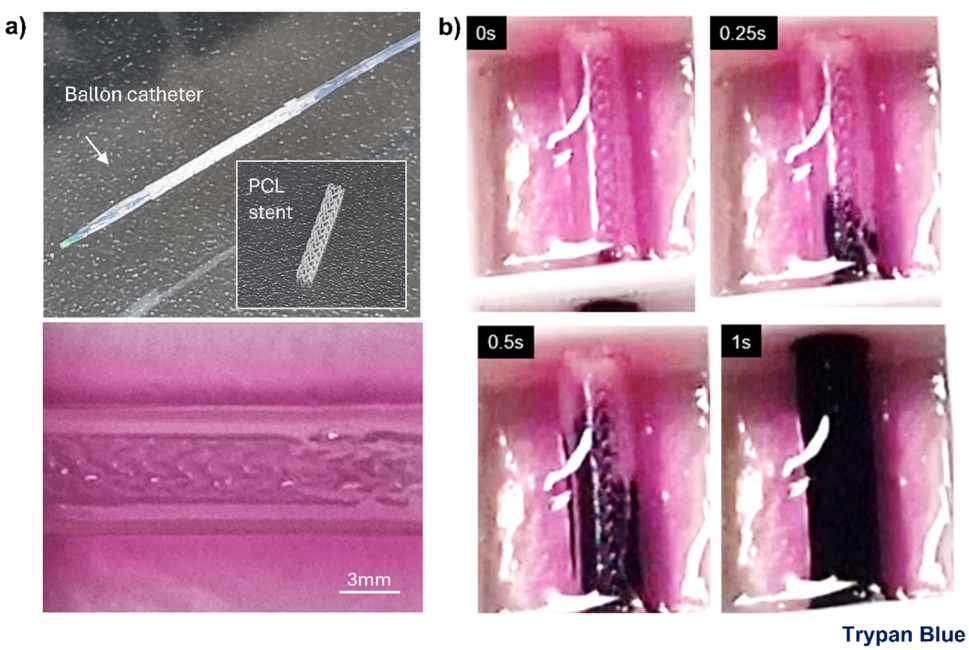

Fig. 6 Stent compatibility of the tube cultured for 3 weeks. (a) An inflatable balloon catheter was used to place a 3 mm PCL stent inside the tube. (b) No leakage was detected during trypan blue perfusion through the tube after stent placement.

pumpless perfusion system, we aimed to assess how closely this setup replicates physiological WSS. CFD analysis revealed that the maximum WSS along the walls of the tube varied between 13 and 14 dyne cm^{-2} at the maximum media reservoir level, across various tilt angles (Fig. S2, ESI†), which falls within the physiological range previously reported (0–40 dyne cm^{-2}).[34,56] The WSS level declines steadily once the media drains to the opposing reservoir. While the tilt angle influences WSS, the range of adjustment is limited because the flow is driven by gravity. A major limitation of our pumpless system is its inability to replicate the unidirectional flow characteristic of native arteries. Thus, while partially mimicking native arterial flow, our system does not fully recapitulate physiological hemodynamic features. Future development of our model will focus on incorporating a recirculating perfusion system to establish unidirectional flow within the tube, thereby enhancing the physiological relevance of the model for arterial hemodynamics.

4. Conclusion and outlook

Most current vascular *in vitro* models, such as microfluidic chips,[27,57–59] hydrogel casting around molds,[60] cell-sheet rolling,[61] and bioprinting,[34,44,62] have effectively demonstrated the recapitulation of vascular physiology. However, most models focused on achieving physiological function rather than recapitulating the size of HCA. For example, microfluidic chips have been able to model the barrier function of vessels in micro-sized channels.[59] Similarly, bioprinted freestanding vessels with an internal diameter of ~1 mm have recapitulated the pathophysiology of arteries, including endothelial dysfunction, monocyte adhesion, and inflammatory responses.[34] These models are promising for advancing drug discovery against vascular pathologies.

However, following the emergence of smart cardiovascular stents designed for specific sizes,[15,17] there is a need for HCA-sized models that can accommodate these stents. While some efforts have been made to fabricate stentable arteries, they could not demonstrate that they can recapitulate HCA dimensions and endothelium barrier functionality.[63] To the best of our knowledge, no reports exist on the successful replication of HCA dimensions using bioprinting technology.

Anatomically, the HCA consists of three layers: the innermost tunica intima, middle tunica media, and the outer tunica adventitia.[64] The tunica intima is lined with endothelial cells that form a monolayer, which plays a pivotal role in the pathogenesis of coronary artery pathologies.[65] Dysfunction of endothelium leads to early stages of atherosclerosis and plaque development. Therefore, engineering the endothelium is of utmost importance in tissue-engineered blood vessels pertaining to applications for intravascular devices such as stents. To address this, we utilized a coaxial nozzle capable of simultaneously depositing two materials concentrically. We developed a bioink composed of collagen, an abundant protein in vascular tissue,[44] to provide biological relevance, and used alginate to achieve enhanced viscosity and printability. Rapid crosslinking of alginate was facilitated by exposing it to calcium ions flowing simultaneously through the core nozzle, resulting in a highly tubular structure without the risk of collapsing. One challenge in fabricating thick-walled structures is the limited diffusion of alginate crosslinkers that leads to un-gelled alginate on the outer side. We overcame this by using a thermoreversible bath mixed with calcium ions. This core-bath-assisted crosslinking mechanism yields robust tubular structures with controllable wall thickness and internal diameter.

Direct cell printing approaches involve cell-laden bioinks, exposing cells to pneumatic pressure which can cause cell injury or death.[53] Additionally, engineering a two-dimensional endothelium monolayer requires a precise balance between the stiffness and printability of the bioink when laden with cells. We fabricated an acellular tube and endothelialized it, thus avoiding pneumatic-pressure-induced cell damage and bioink tuning complexities. While our bioink was optimized for controlled dimensions, the dissociation of sodium alginate over time during culture led to a loss of mechanical strength, making the structure fragile. To provide support, we employed a GelMA matrix, known for its slow degradation, good mechanical properties, and high-optical transparency.[66] This allowed the tracking of molecular permeability across the endothelium to the perivascular region.

To further reduce the complexity of the culture process, a pumpless perfusion platform was employed, which enables a gravity-driven flow and thus eliminates the need for specialized equipment such as pumps to provide hemodynamic cues.[50] Although it can only partially mimic the native flow, it is anticipated that future research focused on developing recirculating flow using pumpless models will enhance the feasibility of these platforms. The compatibility of the HCA-sized tubular structure with stents, as demonstrated in this study, indicates its potential as a valuable tool in the development of novel drug-eluting and smart stents.

Data availability

The data supporting this article have been included as part of the ESI.†

Conflicts of interest

There are no conflicts to declare.

Acknowledgements

This work was supported by the National Research Foundation of Korea (NRF) grants funded by the Korea government (Ministry of Science and ICT, MSIT) [No. NRF-2019R1C1C1009606; No. 2020R1A5A8018367; and No. RS-2024-00423107]. This research was supported by the Bio and Medical Technology Development Program of the NRF grants funded by the MSIT [No. NRF-2022M3A9E4017151 and No. NRF-2022M3A9E4082654].

This work was supported by the Technology Innovation Program [No. 20015148] and the Alchemist Project [No. 20012378] funded by the Ministry of Trade, Industry and Energy (MOTIE, Korea). This work was also supported by the Korea Institute of Planning and Evaluation for Technology in Food, Agriculture and Forestry (IPET) through the Agriculture and Food Convergence Technologies Program for Research Manpower development, funded by the Ministry of Agriculture, Food and Rural Affairs (MAFRA) [No. RS-2024-00397026].

References

1 S. Bansilal, *Int. J. Cardiol.*, 2015, **201**, S1–S7.
2 S. Islam, F. Nobel, S. Sabrina, A. Islam and M. Islam, *J. Adv. Biotechnol. Exp. Ther.*, 2023, **6**, 25.
3 P. Libby, *Sci. Am.*, 2002, **286**, 46.
4 K. Sakakura, M. Nakano, F. Otsuka, E. Ladich, F. D. Kolodgie and R. Virmani, *Heart, Lung Circ.*, 2013, **22**, 399.
5 J. Henriques, A. M. Amaro and A. P. Piedade, *Polymers*, 2023, **15**, 480.
6 I. Hetherington, *Mol. Ther.*, 2022, **30**, 3106–3117.
7 P. Lylyk, J. E. Cohen, R. Ceratto, A. Ferrario and C. Miranda, *AJNR Am. J. Neuroradiol.*, 2002, **23**, 430–436.
8 N. L. Mills and C. T. Everson, *J. Thorac. Cardiovasc. Surg.*, 1991, **102**, 546.
9 M. Marzilli, C. N. B. Merz, W. E. Boden, R. O. Bonow, P. G. Capozza, W. M. Chilian, A. N. DeMaria, G. Guarini, A. Huqi and D. Morrone, *et al.*, *J. Am. Coll. Cardiol.*, 2012, **60**, 951.
10 R. Khan, V. Spagnoli, J.-C. Tardif and P. L. L'Allier, *Atherosclerosis*, 2015, **240**, 497.
11 M. W. Liu, G. S. Roubin and S. B. King, *Circulation*, 1989, **79**, 1374.
12 V. Farooq, B. D. Gogas and P. W. Serruys, *Circ.: Cardiovasc. Interventions*, 2011, **4**, 195.
13 R. G. Geocadin, *JAMA Netw. Open*, 2020, **3**, e208809.
14 N. Berg, *Flow, Turbul. Combust.*, 2019, **102**, 27–41.
15 D.-S. Kim, N.-E. Oyunbaatar, A. Shanmugasundaram, Y.-J. Jeong, J. Park and D.-W. Lee, *Analyst*, 2022, **147**, 4793.
16 R. Tung, S. Kaul, G. A. Diamond and P. K. Shah, *Ann. Intern. Med.*, 2006, **144**, 913.
17 N.-E. Oyunbaatar, D.-S. Kim, G. Prasad, Y.-J. Jeong and D.-W. Lee, *Sens. Actuators, A*, 2022, **346**, 113869.
18 L. Polonchuk, M. Chabria, L. Badi, J.-C. Hoflack, G. Figtree, M. J. Davies and C. Gentile, *Sci. Rep.*, 2017, **7**, 7005.
19 R. J. Wall and M. Shani, *Theriogenology*, 2008, **69**, 2.
20 A. M. Carter, *Placenta*, 2007, **28**, S41.
21 B. C. Hodgkin, D. E. Burkett and E. B. Smith, *Am. J. Physiol.: Heart Circ. Physiol.*, 1982, **242**, H127.
22 C. J. Van Andel, P. V. Pistecky and C. Borst, *Ann. Thorac. Surg.*, 2003, **76**, 58.
23 A. Shah, C. E. Goerlich, C. Pasrija, J. Hirsch, S. Fisher, P. Odonkor, E. Strauss, D. Ayares, M. M. Mohiuddin and B. P. Griffith, *JACC: Case Rep.*, 2022, **4**, 1049.
24 R. Portillo-Lara, A. R. Spencer, B. W. Walker, E. Shirzaei Sani and N. Annabi, *Biomaterials*, 2019, **198**, 78.
25 P. Losi, L. Mancuso, T. Al Kayal, S. Celi, E. Briganti, A. Gualerzi, S. Volpi, G. Cao and G. Soldani, *Biomed. Mater.*, 2015, **10**, 045014.
26 I. Orellano, A. Thomas, A. Herrera, E. Brauer, D. Wulsten, A. Petersen, L. Kloke and G. N. Duda, *Adv. Funct. Mater.*, 2022, **32**, 2208325.
27 A. Günther, S. Yasotharan, A. Vagaon, C. Lochovsky, S. Pinto, J. Yang, C. Lau, J. Voigtlaender-Bolz and S.-S. Bolz, *Lab Chip*, 2010, **10**, 2341.
28 M. H. Rambøl, J. Hisdal, J. O. Sundhagen, J. E. Brinchmann and A. Rosales, *EBioMedicine*, 2018, **32**, 215.
29 R. Mahajan B, A. Atmaram A, P. Meshram, N. V. Ranadhir and S. Hattangadi, *Heart Vvessels Transplant.*, 2022, **6**, 172.
30 M. Alhassen, A. Abdalla, M. Akeel and T. Ali, *J. Hypertens. Cardiol.*, 2021, **3**, 1.
31 J. Al Suwaidi, P. B. Berger and D. R. Holmes, Jr., *JAMA*, 2000, **284**, 1828.
32 J. Butany, *J. Clin. Pathol.*, 2005, **58**, 795.
33 E. Claes, J. M. Atienza, G. V. Guinea, F. J. Rojo, J. M. Bernal, J. M. Revuelta and M. Elices, in *2010 Annual International Conference of the IEEE Engineering in Medicine and Biology*, IEEE, Buenos Aires, 2010, pp. 3792–3795.
34 G. Gao, J. Y. Park, B. S. Kim, J. Jang and D. Cho, *Adv. Healthcare Mater.*, 2018, **7**, 1801102.
35 P. Rajendran, T. Rengarajan, J. Thangavel, Y. Nishigaki, D. Sakthisekaran, G. Sethi and I. Nishigaki, *Int. J. Biol. Sci.*, 2013, **9**, 1057.
36 H.-Q. Xu, J.-C. Liu, Z.-Y. Zhang and C.-X. Xu, *Mil. Med. Res.*, 2022, **9**, 70.
37 A. G. Tabriz, M. A. Hermida, N. R. Leslie and W. Shu, *Biofabrication*, 2015, **7**, 045012.
38 Q. Gao, B.-S. Kim and G. Gao, *Mar. Drugs*, 2021, **19**, 708.
39 L. K. Narayanan, P. Huebner, M. B. Fisher, J. T. Spang, B. Starly and R. A. Shirwaiker, *ACS Biomater. Sci. Eng.*, 2016, **2**, 1732.
40 A. D. Augst, H. J. Kong and D. J. Mooney, *Macromol. Biosci.*, 2006, **6**, 623.
41 J. A. Rowley, G. Madlambayan and D. J. Mooney, *Biomaterials*, 1999, **20**, 45.
42 Y. Wen, X. Chen, H. Yan and Q. Lin, *Gels*, 2022, **8**, 799.
43 M. I. Neves, L. Moroni and C. C. Barrias, *Front. Bioeng. Biotechnol.*, 2020, 8.
44 G. Gao, J. H. Lee, J. Jang, D. H. Lee, J.-S. Kong, B. S. Kim, Y.-J. Choi, W. B. Jang, Y. J. Hong and S.-M. Kwon, *et al.*, *Adv. Funct. Mater.*, 2017, **27**, 1700798.
45 Z. Tian, W. Liu and G. Li, *Polym. Degrad. Stab.*, 2016, **130**, 264.
46 D. E. Solomon, *Int. J. Exp. Pathol.*, 1992, **73**, 491.
47 E. O. Osidak, E. P. Kalabusheva, E. V. Alpeeva, S. I. Belousov, S. V. Krasheninnikov, T. E. Grigoriev, S. P. Domogatsky, E. A. Vorotelyak and E. S. Chermnykh, *Materialia*, 2021, **20**, 101217.
48 K. Hölzl, S. Lin, L. Tytgat, S. V. Vlierberghe, L. Gu and A. Ovsianikov, *Biofabrication*, 2016, **8**, 032002.
49 P. D. Williams, N. Malik and P. A. Kingston, *Animal*, 2012, **6**, 311.

50 P. Nagathan, A. Patil, S. C. Desai, C. Rajashekhar, I. Sarris, H. Vaidya and K. V. Prasad, *Int. J. Appl. Comput. Math.*, 2022, **8**, 151.
51 Y. Z. Zhang, J. Venugopal, Z.-M. Huang, C. T. Lim and S. Ramakrishna, *Biomacromolecules*, 2005, **6**, 2583.
52 F. Liu, C. Vyas, G. Poologasundarampillai, I. Pape, S. Hinduja, W. Mirihanage and P. Bartolo, *Macromol. Mater. Eng.*, 2018, **303**, 1700494.
53 S. Boularaoui, G. Al Hussein, K. A. Khan, N. Christoforou and C. Stefanini, *Bioprinting*, 2020, **20**, e00093.
54 Y. S. Chang, L. L. Munn, M. V. Hillsley, R. O. Dull, J. Yuan, S. Lakshminarayanan, T. W. Gardner, R. K. Jain and J. M. Tarbell, *Microvasc. Res.*, 2000, **59**, 265.
55 H. Yu, D. Kang, M. Whang, T. Kim and J. Kim, *Adv. Healthcare Mater.*, 2021, **10**, 2100508.
56 K. S. Cunningham and A. I. Gotlieb, *Lab. Invest.*, 2005, **85**, 9.
57 Z. Liao, J. Wang, P. Zhang, Y. Zhang, Y. Miao, S. Gao, Y. Deng and L. Geng, *Biosens. Bioelectron.*, 2018, **121**, 272.
58 M. Raasch, K. Rennert, T. Jahn, S. Peters, T. Henkel, O. Huber, I. Schulz, H. Becker, S. Lorkowski and H. Funke, *et al.*, *Biofabrication*, 2015, **7**, 015013.
59 E. W. K. Young, M. W. L. Watson, S. Srigunapalan, A. R. Wheeler and C. A. Simmons, *Anal. Chem.*, 2010, **82**, 808.
60 A. W. Justin, R. A. Brooks, A. E. Markaki and J. R. Soc, *Interface*, 2016, **13**, 20160768.
61 S. Rayatpisheh, D. E. Heath, A. Shakouri, P.-O. Rujitanaroj, S. Y. Chew and M. B. Chan-Park, *Biomaterials*, 2014, **35**, 2713.
62 X. Dai, L. Liu, J. Ouyang, X. Li, X. Zhang, Q. Lan and T. Xu, *Sci. Rep.*, 2017, **7**, 1457.
63 E. E. Antoine, F. P. Cornat and A. I. Barakat, *J. R. Soc., Interface*, 2016, **13**, 20160834.
64 H. J. Carpenter, A. Gholipour, M. H. Ghayesh, A. C. Zander and P. J. Psaltis, *Int. J. Eng. Sci.*, 2020, **147**, 103201.
65 J. Davignon and P. Ganz, *Circulation*, 2004, **109**, III.
66 A. Farasatkia, M. Kharaziha, F. Ashrafizadeh and S. Salehi, *Mater. Sci. Eng., C*, 2021, **120**, 111744.